Sensors and Actuators A 217 (2014) 151–159

Contents lists available at ScienceDirect

Sensors and Actuators A: Physical

journal homepage: www.elsevier.com/locate/sna

100 GHz ultra-high Q-factor photonic crystal resonators

William J. Otter[a,b,*], Stephen M. Hanham[a,c], Nick M. Ridler[d], Giuseppe Marino[e], Norbert Klein[a,c], Stepan Lucyszyn[a,b]

[a] Centre for Terahertz Science and Engineering, Imperial College London, UK
[b] Optical and Semiconductor Devices Group, Electrical and Electronic Engineering, Imperial College London, UK
[c] Department of Materials, Imperial College London, UK
[d] National Physical Laboratory, Teddington, London, UK
[e] Dipartimento di Fisica e Astronomia, Università degli Studi di Catania, Catania, Italy

ARTICLE INFO

Article history:
Received 7 March 2014
Received in revised form 25 June 2014
Accepted 25 June 2014
Available online 11 July 2014

Keywords:
Photonic crystal
Resonator
Q-factor
Electromagnetic band gap
Bulk micromachining
Silicon

ABSTRACT

We demonstrate an ultra-high Q-factor photonic crystal resonator operating in the millimeter-wave band, which is suitable for use as an integrated sensing platform. Experimental results show that at 100 GHz a loaded Q-factor of 5 000 and 8 700 can be achieved with a strongly and weakly coupled cavity design, respectively. The uncertainty in the experimental results has been analyzed and a new technique of propagating uncertainty in *S*-parameter measurements for the determination of Q-factor is given. The result of this uncertainty analysis gives an unloaded Q-factor of 9 040 ± 300; being fundamentally limited to ~10 000 by the intrinsic dielectric loss of the high resistivity silicon substrate. Utilizing standard bulk-micromachining of silicon, the resonators can be monolithically integrated into RFICs and MMICs for applications including liquid and gas sensing.

© 2014 The Authors. Published by Elsevier B.V. This is an open access article under the CC BY-NC-ND license (http://creativecommons.org/licenses/by-nc-nd/3.0/).

1. Introduction

The millimeter-wave and terahertz regions of the electromagnetic spectrum are of particular interest for sensing due to the abundance of spectroscopic features associated with molecular resonances found throughout these regions [1]. High quality (Q) factor electromagnetic resonators represent an important technology for realization of sensing systems operating in these bands [2,3]. They enable extremely sensitive detection of an analyte's complex permittivity through enhancement of the strength of interaction between the analyte and resonant mode [4].

Beyond sensing, high Q-factor resonators can be used to realize important components for future millimeter-wave and terahertz communication and radar systems, such as low phase noise oscillators and band pass filters.

Conventional room-temperature passive millimeter-wave resonators employing metal cavities or structures are generally limited in their Q-factor by losses associated with the metal features [5,6]. For this reason, dielectric resonators made from low-loss materials are preferred. Additionally, resonators which have a planar form factor are better suited toward system integration and mass production for future lab-on-a-chip devices. In Table 1, we present a summary of the Q-factors achieved by various state-of-the-art W-Band (75–110 GHz) resonators, which could be realized as part of a monolithic microwave integrated circuit (MMIC) [7]. This simple comparison is far from straightforward, as many authors fail to explain the methods used to calculate the Q-factor being quoted; either loaded (Q_L) or unloaded (Q_0).

In this paper we present an ultra-high Q-factor photonic crystal (PC) resonator. The PC has been engineered to have an electromagnetic band gap by periodic arrangement of two dielectric materials with contrasting permittivities. Similar approaches have been successfully applied at optical wavelengths to achieve high Q-factors [12] and their use for sensing has been demonstrated [13–15]; however, such high Q-factors have yet to be proven in the millimeter(mm)-wave band. Previous PC work at microwave and mm-wave frequencies has focused on demonstrating the size of the predicted band gap [16], waveguide structures [17], switches [18] and filters [19,20]; all with low Q-factors.

The specific type of PC developed for this paper has an engineered transverse electric (TE)-like (since the electric field has only in-plane components) electromagnetic band gap, created through a two dimensional periodic triangular lattice of cylinders having a

* Corresponding author at: Optical and Semiconductor Devices Group, Electrical and Electronic Engineering, Imperial College London, UK.
E-mail address: william.otter06@imperial.ac.uk (W.J. Otter).

http://dx.doi.org/10.1016/j.sna.2014.06.022
0924-4247/© 2014 The Authors. Published by Elsevier B.V. This is an open access article under the CC BY-NC-ND license (http://creativecommons.org/licenses/by-nc-nd/3.0/).

Table 1
Previously reported W-band resonator Q-factors.

Resonator Type	Frequency (GHz)	Q-factor
Multiple ring resonator [8]	75	85
Quasi-metallic silicon PC [9]	90	25
Air-filled metal cavity [10]	94	850
Whispering gallery [11]	100	3 020

different dielectric constant to the substrate [21]. The radius of the cylinders, bulk material permittivity, thickness of the bulk material and periodicity can all be optimized in order to shift the location of the band gap. Within the lattice structure, engineered defects can give rise to allowed modes within the band gap, which can be exploited to produce resonant cavities and waveguides.

The high Q-factor resonators presented in this paper have been evaluated through simulation and measured experimental results. A rigorous analysis of the uncertainty in the Q-factor is given. Here, an analysis technique is presented that shows how uncertainty propagates from *S*-parameter measurements to Q-factor. The results clearly show that the PC design has a better performance than alternative state-of-the-art W-band resonator technologies that offer a similar compatibility for the monolithic integration of future sensing systems.

2. Design

The PC in this work is formed from a triangular lattice of air holes in a planar substrate. It is fabricated from a 525 μm thick high resistivity silicon (HRS) substrate (having the real part of the complex effective relative permittivity $\varepsilon'_{reff}(100\ \ \text{GHz}) = 11.64$ [22] and a dc bulk resistivity greater than 10 kΩ cm). The holes have a radius of 235 μm and a lattice constant of 780 μm. The band structure for this geometry was calculated using a plane-wave eigenmode solver [23] and the results for the lowest order modes are shown in Fig. 1. It can be seen that this structure produces an incomplete (TE-like) band gap between 97 and 127 GHz, with a center frequency at 112 GHz and a fractional bandwidth of 26%.

A resonant cavity was created in the photonic crystal by introducing a defect in the lattice; in this case formed by omitting three adjacent holes (called an L3 cavity). The mode inside the

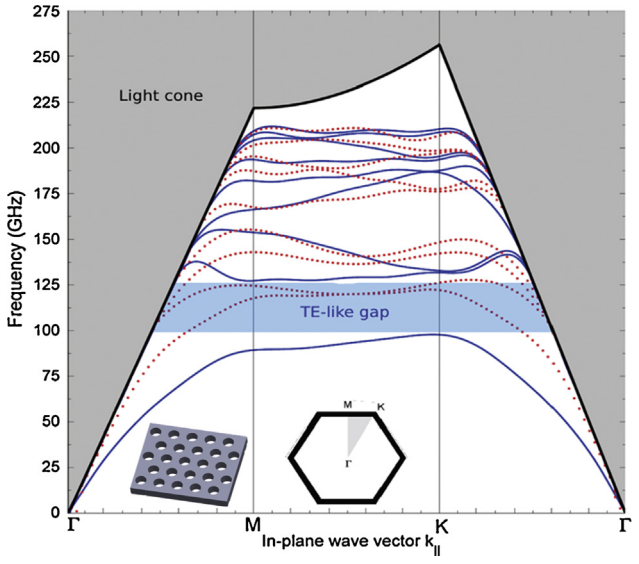

Fig. 1. Band diagram for the photonic crystal design showing the TE-like modes (blue) and TM-like modes (red dashed). The bottom left inset shows the crystal lattice structure and the central bottom inset shows the lattice Brillouin zone with the irreducible region shaded gray. (For interpretation of the references to color in this figure legend, the reader is referred to the web version of this article.)

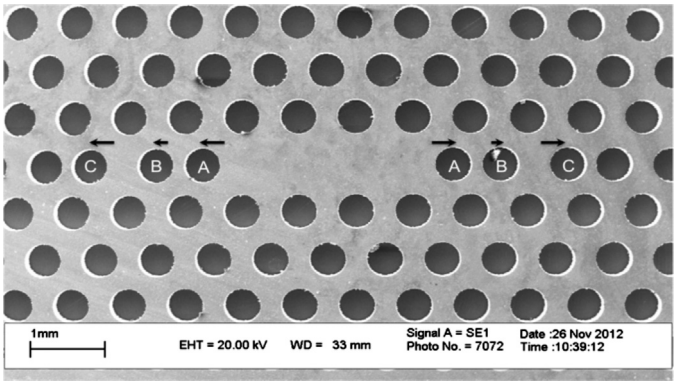

Fig. 2. Fabricated L3 cavity defect. Holes A–C are shifted away from the cavity by 156 μm, 19 μm and 156 μm, respectively.

cavity is confined in-plane by Bragg reflections within the PC and out-of-plane by total internal reflections (TIRs) at the silicon-air interfaces.

It has previously been shown that the positioning of the holes surrounding the cavity is critical to achieving a high-Q resonance, by reducing out-of-plane radiation losses [12]. The adjustment of hole positions at the cavity edge make it possible to more gently confine the fields, allowing them to penetrate further into the crystal. A plane-wave expansion of the fields inside the cavity shows that this delocalization corresponds to a narrowing in the spatial spectral domain. This narrowing reduces components of the in-plane wave-vector $k_{\|}$ that do not satisfy the condition for TIR (i.e. $0 < k_{\|} \leq 2\pi/\lambda_0$, where λ_0 is the free-space wavelength) and thereby contribute to radiation loss. Further details of this effect can be found in [12,24]. To minimize radiation losses in our design, the three holes on each side adjacent to the cavity (starting from the closest hole) were shifted 156 μm, 19 μm and 156 μm away from the cavity, in relation to their normal lattice positions, as is shown in Fig. 2.

To couple energy into the cavity, a W1 defect feed waveguide was created by omitting a partial row of adjacent holes in the PC lattice. Three different W1 defect waveguide configurations were considered – one with the W1 defect feed waveguides inline below the cavity. The other two have the feed waveguides offset above and below the cavity, to reduce mutual coupling. With the offset configuration, two different lengths of W1 waveguide were considered, to provide weak and strong coupling to the cavity, as shown in Fig. 3. A weak coupling provides a better estimation of the unloaded Q-factor as $Q_0 = Q_L/(1-\kappa)$ [25], where Q_L is the loaded Q-factor and $\kappa = |S_{21}|$ where κ is the coupling factor. This means that for the weakly coupled PC with a resonant peak at −40 dB, Q_L will be within 1% of Q_0.

To couple a TE-like mode into the W1 defect feed waveguide, a triangular taper is created at the edge of the substrate, so that it can align to and fit inside a standard WR10 waveguide aperture [26], as illustrated in Fig. 4. The triangular taper was 2.1 mm long

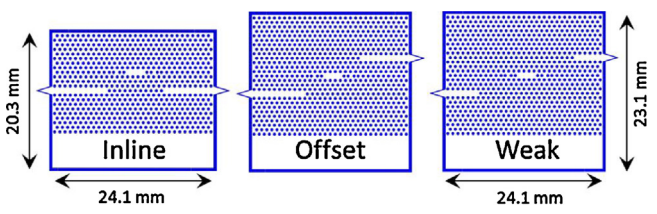

Fig. 3. Three PC resonator designs with the blue dots denoting air holes in the white HRS substrate. The left design has the excitation W1 defect feed waveguides inline and the other two have the offset configuration. The resonator on the right is weakly coupled, while the other two are strongly coupled.

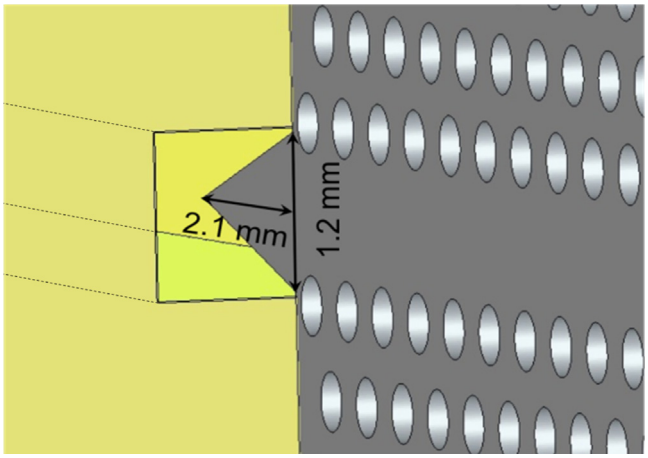

Fig. 4. Illustration showing how the solid triangular silicon taper fits inside the WR10 waveguide in the E-plane at the center of the aperture.

and 1.2 mm high, optimized to ensure a smooth transition from the WR10 waveguide TE_{10} mode to the TE-like W1 defect feed waveguide mode.

3. Simulation results

Initial full-wave simulations were performed using CST Microwave Studio® to confirm the TE-like band gap. A lattice of 11 horizontal rows of either 20 or 21 air holes in the HRS substrate was modeled to observe the TE-like band gap. Here, the open boundary condition (with free space surrounding the structure) was used as the global boundary condition. The simulated structure was excited with the fundamental TE_{10} mode of the WR10 waveguide with the WR10 waveguide flange included, so that diffraction around the walls of the waveguide was reduced. Fig. 5 shows that the band gap is observed between 97 and 127 GHz, in good agreement with the calculations shown in Fig. 1. The electric field magnitude plots presented in Fig. 5 show that outside the PC band gap the field propagates in all directions through the lattice; within the band gap there is no propagation through the lattice.

Numerical simulations were run with both strongly coupled PC designs for the entire structure; although sufficient computing power was not available to run the weakly coupled designs. The simulations were initially performed with the silicon having a loss tangent of zero. The resulting *S*-parameters, shown in Fig. 6, show the sharp resonances as expected. A frequency shift is observed between the two resonator designs, despite the cavities having the same dimensions. This is caused by the different meshes created

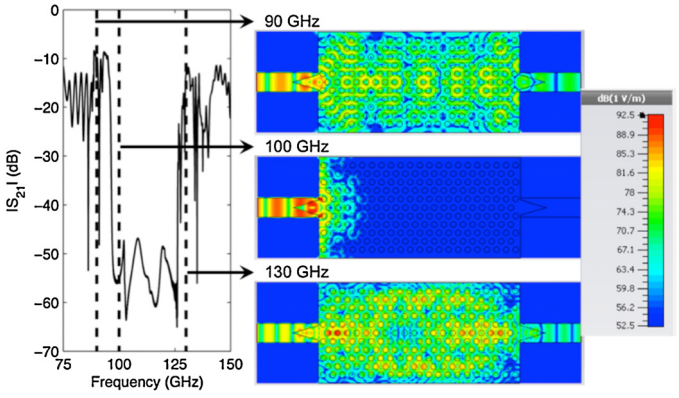

Fig. 5. Simulated transmission demonstrating the band gap with corresponding electric field plots.

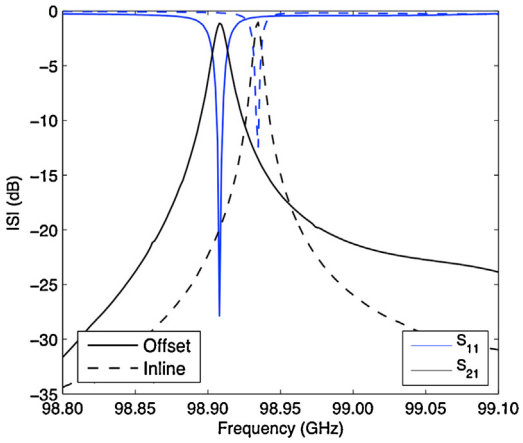

Fig. 6. Simulated *S*-parameters for strongly coupled PC resonators having zero effective loss tangent silicon.

by the simulation solver. This could not be further refined, due to our limitations in computational resources (currently having twelve 3 GHz cores and 128 GB of RAM). The introduction of dielectric losses, having an effective loss tangent of tan $\delta_e \sim 10^{-4}$ for a HRS resistivity of 10 kΩ cm [21], causes the insertion losses to increase and a broadening of the resonant peaks, as shown in Fig. 7. This demonstrates that the Q-factor of these structures will be ultimately limited by dielectric losses.

Fig. 8 shows the E-field magnitude within the PC resonator when the cavity is off-resonance and at resonance, respectively. It clearly illustrates how the energy is coupled through the cavity from the input to the output W1 defect waveguide and the enhancement of the field inside the cavity.

4. Fabrication

The PC resonators were fabricated from 100 mm diameter HRS wafers of thickness 525 μm ± 5 μm with resistivity >10 kΩ cm. HRS wafers were chosen due to their low effective loss tangent and high permittivity at 100 GHz [21], their compatibility with integrated RF CMOS electronics and inherent compatibility with bulk micromachined RF MEMS (radio frequency microelectromechanical systems) [27].

Fig. 9 shows the process flow for fabricating the PC resonators. The first step is cleaning the wafer to remove any surface particles. An adhesion promoting layer (TI PRIME) is then spun on, followed by a 10 μm thick layer of photoresist (AZ9260). This photoresist layer is sufficient to be used as a soft mask for thru-wafer deep

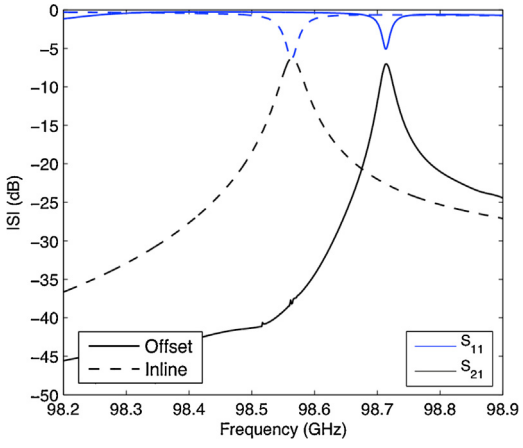

Fig. 7. Simulated *S*-parameters for strongly coupled PC resonators with tan $\delta_e = 10^{-4}$.

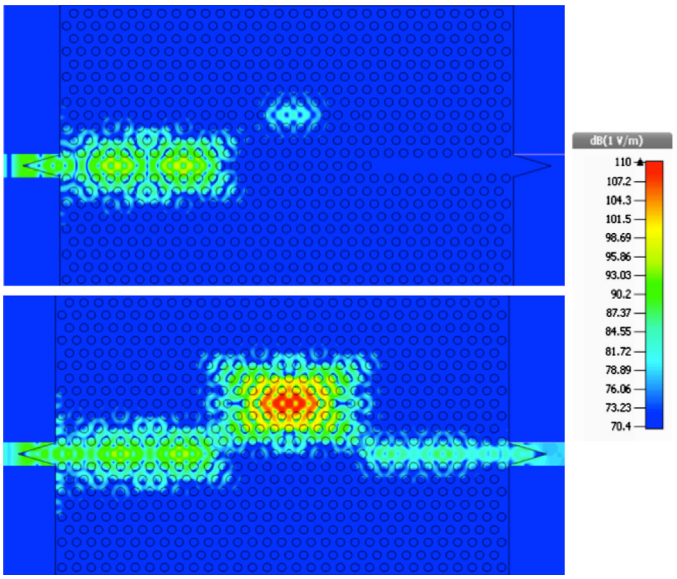

Fig. 8. E-field magnitude plots showing the cavity excited away from resonance (above) and at resonance (below).

reactive-ion etching (DRIE) of the 525 μm thick HRS substrate, as it has a preferential etch selectivity of 80:1 [28]. The PC pattern is transferred into the photoresist using standard photolithographic techniques with a single low-cost acetate mask.

Once the photoresist is fully developed, the wafer is placed within the DRIE system, where the sample is etched using the Bosch process. This involves alternating between a plasma etch of SF_6 and then depositing a passivation layer of C_4F_8. This cycle of etch-and-passivation continues until the wafer has been etched to two thirds of its total thickness. At this stage a backing wafer is applied to prevent damage to the DRIE system's chuck. A single-sided, polished 100 mm diameter low-resistivity silicon (LRS) wafer is used for the backing wafer, as it is low cost and compatible with DRIE. To form a temporary attachment to the HRS wafer, a thermally conducting paste (TCP) is used. The TCP ensures that the heat generated by DRIE is transferred away from the top HRS wafer being etched to the backing LRS wafer that is helium cooled. This avoids

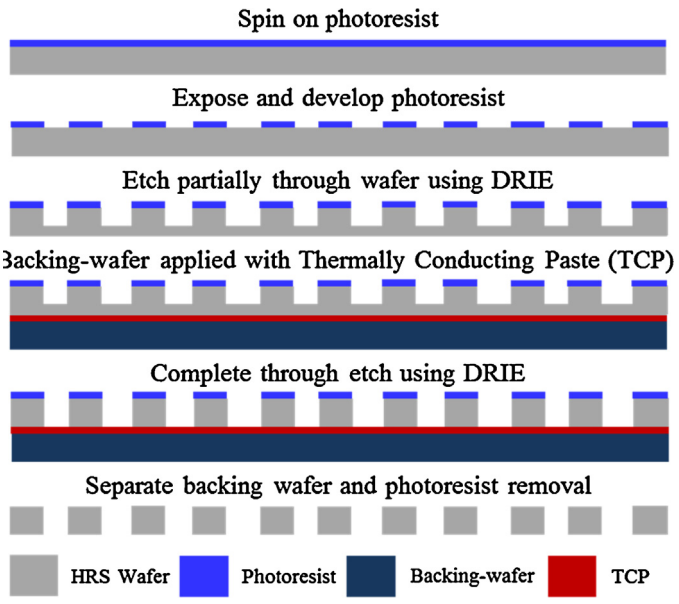

Fig. 9. Microfabrication processing steps for the PC.

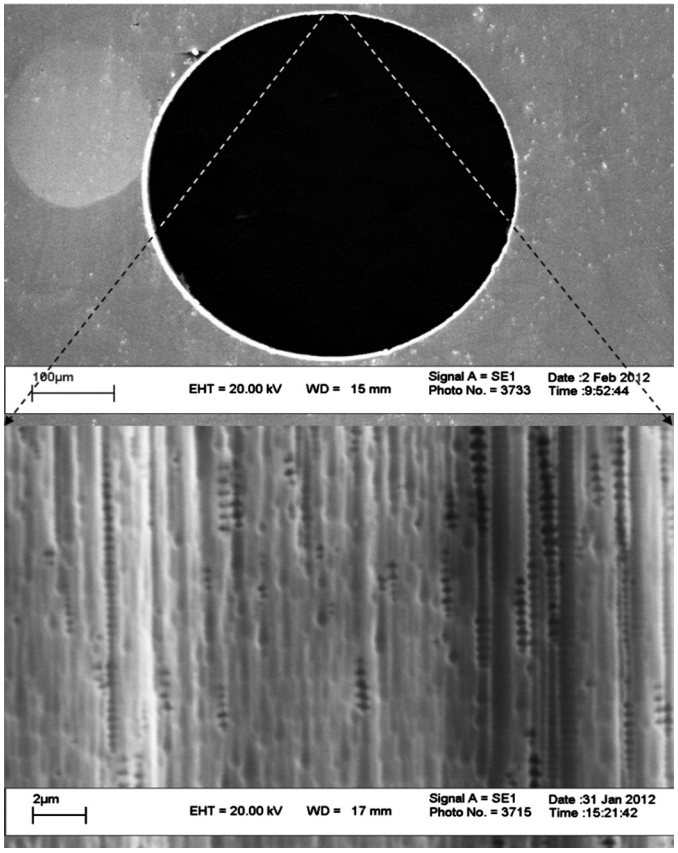

Fig. 10. Etched hole viewed from above (top) and typical sidewall profile (bottom).

the photoresist burning, as this would reduce its selectivity to DRIE and could lead to etching of the top surface of the silicon.

Once the HRS wafer (with the LRS backing wafer still in place) has been etched through, it is visually inspected to confirm that thru-wafer etching has been completed. The backing wafer is then mechanically removed. The TCP and remaining photoresist are removed with isopropanol, acetone and deionized water.

Fig. 10 shows the final results of the etching process. It can be seen that the holes exhibit good roundness. A close-up image of one of the holes' sidewall reveals that some surface roughness exists, as expected. This is due to the imperfect circular definition of the acetate mask used, where any defect is propagated down the sidewall of the structure. In future, this could be improved through the use of a more expensive chrome-on-glass mask.

Various other fabrication methods have been proposed for the creation of photonic crystals. For example, in [29] an alternate approach uses a silicon oxide mask; however, this adds further processing steps to grow, pattern and remove the oxide. This method also adds further complications, since a photoresist mask is still required to pattern the oxide layer. Moreover, the high temperatures required to grow a thick thermal oxide layer can potentially introduce significant unwanted charge carriers and, thus, compromise the high resistivity nature of the HRS.

5. Experimental results

S-parameter measurements were carried out using a vector network analyzer (VNA) configured with a pair of WR10 waveguide frequency multiplier heads that cover the complete W-band (i.e. from 75 to 110 GHz).

Measurements were undertaken by first performing a thru-reflect-line (TRL) calibration [30] at the waveguide frequency

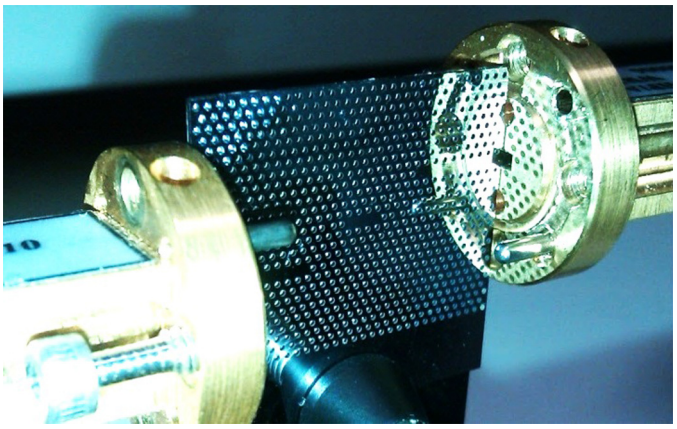

Fig. 11. Experimental measurement setup showing how the PC resonator devices are mounted between two WR10 rectangular waveguide frequency multiplier heads.

multiplier head reference planes. The calibration employed WR10 waveguide standards: a thru connection; a quarter-wavelength section of line, to provide a 90° phase change in the middle of the waveguide band (with a waveguide length of approximately 1.08 mm); and a flush short-circuit as the reflect standard connected in turn to each reference plane. The calibration was performed using an external calibration algorithm, employing a seven-term error-correction routine [31]. The overall set-up (i.e. VNA, primary standards and calibration algorithm) is referred to as the NPL Primary Impedance Microwave Measurement System (PIMMS) [32,33]. This is the UK's primary national standard system for *S*-parameter measurements and is described in [34] for millimeter-wave waveguide measurements.

For resonator device measurement, the PC coupling taper was aligned with the center of each waveguide frequency multiplier head, penetrating inside the waveguide aperture so that the crystal sat flush with the waveguide flange, as shown in Fig. 11. The fabricated resonators differ slightly from the simulated structures; an extra extension of bulk HRS substrate was added to the bottom of the PC, so that the structure could be physically held in position and accurately aligned using a micrometer-controlled linear stage.

Fig. 12 shows a broadband transmission sweep of a single PC resonator, from 85 to 110 GHz with a frequency sample interval of 100 MHz. The expected band gap of the PC is clearly seen by the 20 dB drop in transmission above 96 GHz extending to the 110 GHz

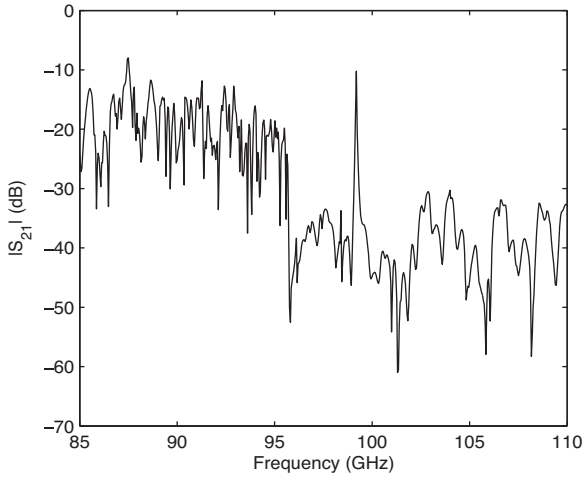

Fig. 12. Broadband transmission response showing the resonance of a strongly coupled 99 GHz offset PC resonator.

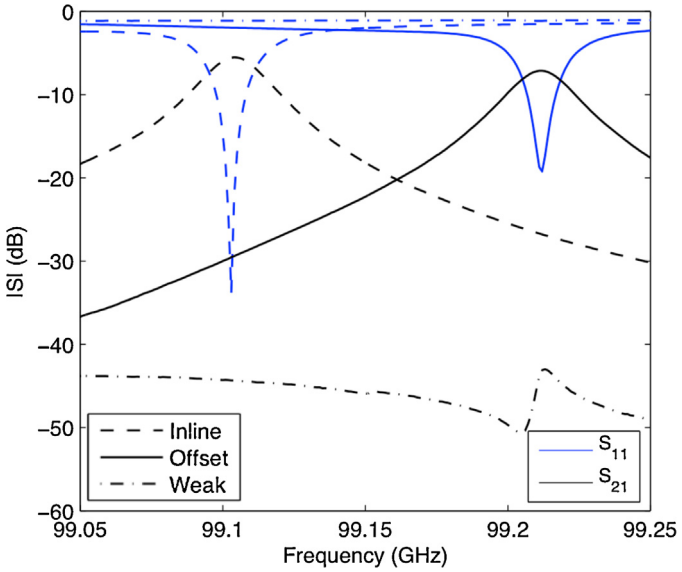

Fig. 13. Measured *S*-parameter magnitude responses for the PC resonators close to the resonant frequency.

recommended measurement limit for the WR10 waveguide. The peak at approximately 99 GHz is the resonance caused by the cavity; the full peak is not seen due to the coarse frequency sampling interval.

Figs. 13 and 14 show the measured $|S_{11}|$, $|S_{21}|$ and $\angle S_{21}$ responses between 99.05 and 99.25 GHz, with 1 MHz resolution, for the three manufactured resonators illustrated in Fig. 3.

It has been found that the variations in the insertion and return losses, between the two strongly coupled PC resonators, is due to the mechanical alignment between the PC tapers and the center of the WR10 waveguide apertures. Therefore, this is not an inherent limitation, as there is a great deal of scope to create mechanically and electromagnetically optimal transitions between a calibration reference plane and the associated W1 defect feed waveguide for such ultra-high Q-factor DUT (device under test).

The weakly coupled resonator has a resonance peak and phase slope that are differing in shape, when compared to the strongly coupled resonators. This is because the peak at −45 dB is the result

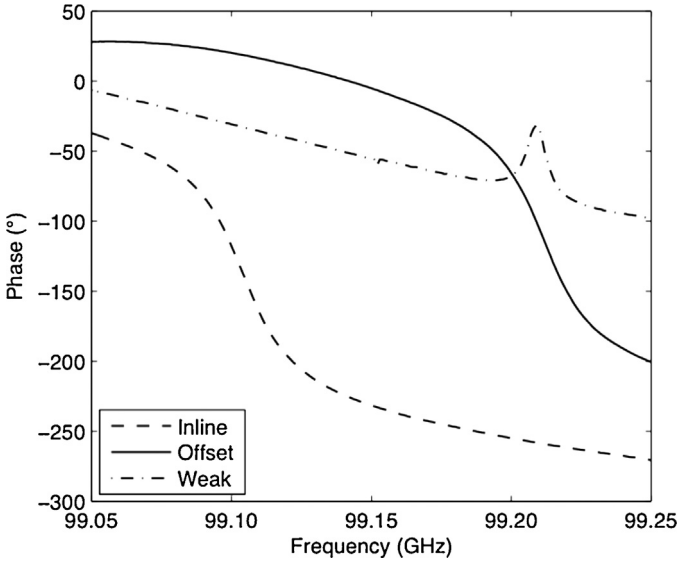

Fig. 14. Measured transmission phase responses for the PC resonators close to the resonant frequency.

Table 2
Simulated Q-factors.

Resonator	3 dB Q_L	Phase Q_L	3 dB Q_0	Phase Q_0
Lossless offset	8 830	8 860	72 330	72 550
Lossless inline	10 370	10 440	91 750	92 370
Lossy offset	4 550	4 800	8 190	8 640
Lossy inline	4 840	5 010	9 420	9 750

of the superposition from the resonant cavity and other coupling paths (as seen in Fig. 12), which are at a comparable level.

Also of note is a slight variation of resonant frequency across the fabricated PCs, from 99.10 to 99.22 GHz (i.e. 0.12%). This is believed to be caused by variations in the DRIE etch across the wafer and hole size; simulations show that an increase in hole diameter will increase the resonant frequency. To minimize this variation, the bulk micromachining process could be modified; for example, a chrome-on-glass mask or packing pieces could be employed. The former has a greater resolution, giving better defined circles [28].

6. Q-factor determination

From circuit analysis of *RLC* tuned circuit resonators, there are two methods to calculate the loaded Q-factor (Q_L) of a resonator, and a basic formula to determine the unloaded Q-factor (Q_0) from Q_L. It is well known that Eq. (1) defines how Q_L is obtained using the −3 dB bandwidth, where f_0 is the resonance frequency, f_u and f_l are the upper and lower frequencies, respectively, defined where the power of a signal drops 3 dB below that at resonance. Equally, Eq. (2) defines how Q_L is obtained from $\angle s_{21}$ transmission phase, where $\omega = 2\pi f$. Finally, Eq. (3) is used to extract Q_0.

$$Q_L(f_0) = \frac{f_0}{f_u - f_l} \tag{1}$$

$$Q_L(f_0) = \frac{\omega_0}{2}\left|\frac{\delta\angle\delta_{21}}{\delta\omega}\right|_{\omega=\omega_o} \tag{2}$$

$$Q_0(f_0) = \frac{Q_L(f_0)}{1 - \left|S_{21}(f_0)\right|} \tag{3}$$

The results obtained from the simulated structures and the experimental data were analyzed using these formulae; the results obtained are presented in Tables 2 and 3. The measured unloaded Q-factor varies from 7 140 to 10 200. This variation is to be expected; as previously mentioned, due to the variation in coupling alignment at the WR10 waveguide heads and also the variation of HRS resistivity, which can vary by ±6% [35]. It should be noted that as expected, for the weakly coupled resonators the loaded and unloaded Q-factors are within <1%. The simulated unloaded Q-factors varied from 8 190 to 9 750 for the substrates that included dielectric loss, showing good agreement between the simulated and measured results. The lossless substrate simulated structures have up to ten times greater unloaded Q-factor, showing that the main limitation on achievable Q-factors at this frequency is the dielectric loss, as seen in [11]. It is well known that for dielectric only resonators, the associated dielectric material loss $Q_D \propto (\varphi \tan \delta_e)^{-1}$, where φ is the dielectric filling factor; this yields a fundamental physical limit on the unloaded Q-factor of $Q_0 \sim 10\,000$ at 100 GHz (assuming a filling factor close to unity and $tan\ \delta_e = 10^{-4}$). This loss

Table 3
Measured Q-factors (before uncertainty analysis).

Resonator	3 dB Q_L	Phase Q_L	3 dB Q_0	Phase Q_0
Strong offset	5 220	5 600	10 050	10 200
Strong inline	4 130	4 310	8 790	9 180
Weak offset	7 090	8 720	7 140	8 780

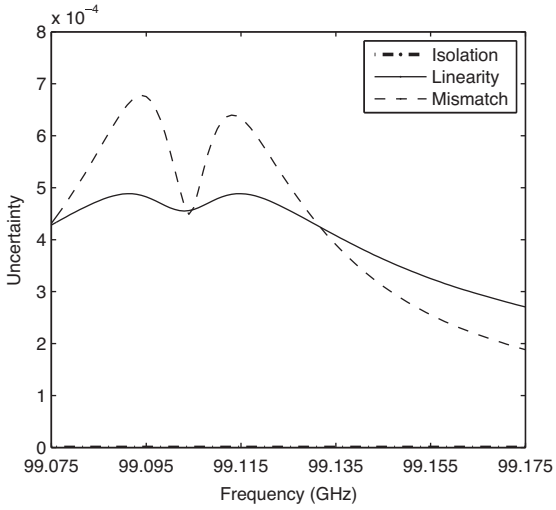

Fig. 15. Type B uncertainty components. The uncertainty in mismatch and linearity dominate while the isolation uncertainty is almost zero.

decreases for HRS as the frequency increases, which explains why PC resonators at higher frequencies can achieve significantly higher Q-factors [12].

To understand the variation in the determination of Q-factor, the overall uncertainty in the measurement setup was evaluated. This was achieved using the strongly-coupled inline PC resonator. The measurement process involved performing a TRL calibration of the VNA and measurement of the PC resonator; this methodology is repeated six times. The data collected along with information describing the performance of the measurement system is used to calculate the overall uncertainty in the measurements [36].

The overall uncertainty represents the uncertainty arising from random effects and from imperfect corrections due to systematic effects. The uncertainty due to the random effects (e.g. due to the repeatability of connections of the PC to the VNA test ports) is evaluated by a statistical analysis of a series of observations. This method is called a Type A evaluation of uncertainty [37].

The uncertainty due to systematic effects (e.g. the VNA linearity, isolation and mismatch between the test ports and the PC DUT) is evaluated by means, other than a statistical analysis, of a series of observations. These (non-statistical) methods of evaluating uncertainty are called Type B [37]. Specifically, the linearity of the VNA is determined by measuring the transmission of a calibrated step attenuator over a range of different attenuator settings. The VNA isolation is determined by observing the measured transmission when no physical connection is made between the test ports. Finally, the mismatch between the VNA and the PC resonator device is determined from the measurements of the *S*-parameters of the PC DUT [36].

Type A uncertainties are intentionally neglected from the following calculations, as it quantifies alignment limitations in our experimental setup and does not change the underlying performance of the PC resonators. Moreover, this is an experimental prototype demonstrator; once monolithically integrated, Type A uncertainties will be significantly reduced and, therefore, only Type B uncertainties need to be taken into consideration here.

Fig. 15 shows the sizes of each of the three Type B uncertainty components – linearity, mismatch and isolation – as a function of frequency. It is seen that, for this measurement set-up, the contribution due to isolation is negligible, (compared with the uncertainty due to linearity and mismatch). This is because there is significant transmission through the PC and so the detected signal level is well above the VNA noise floor. The contributions to uncertainty due to linearity and mismatch are combined to give

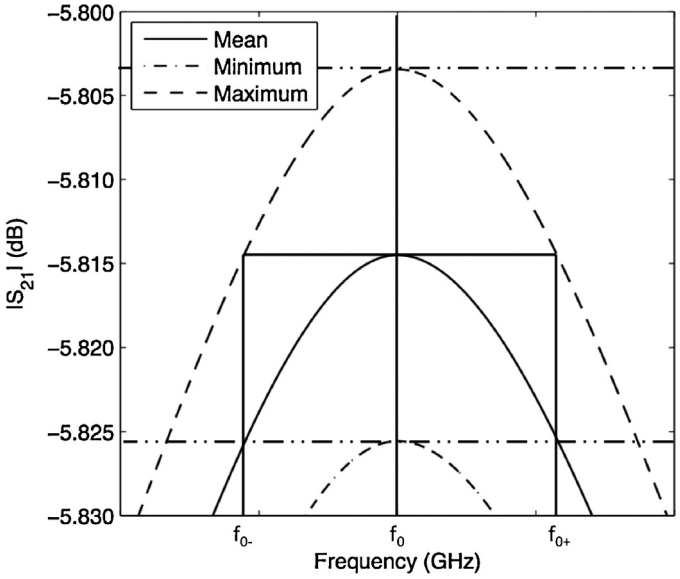

Fig. 16. Impact of uncertainty in $|S_{21}|$ on the determination of f_0 for the strongly-coupled inline PC resonator.

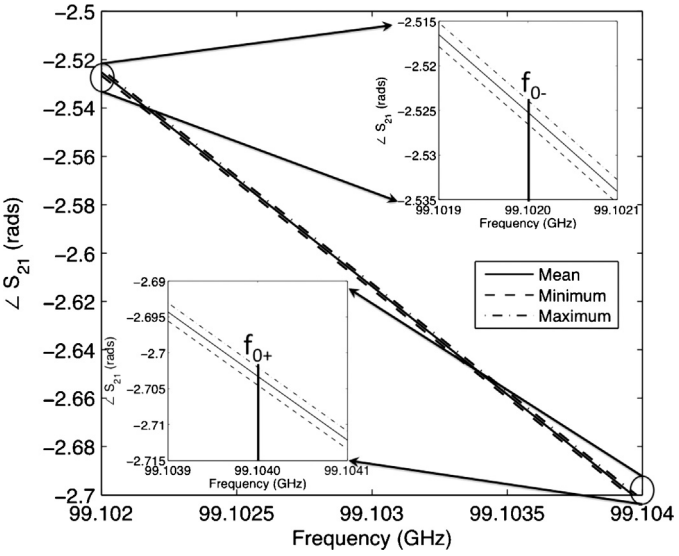

Fig. 18. Impact of uncertainty in $\angle S_{21}$ on the determination on $\left|\frac{\delta \angle S_{21}}{\delta \omega}\right|$ from f_{0+} and f_0 for the strongly-coupled inline PC resonator.

the overall uncertainty in the *S*-parameter measurement results at each measurement frequency.

6.1. Uncertainty analysis for 3 dB Q-factor determination

The uncertainty in the *S*-parameter measurements is propagated to the uncertainty in Q-factor determination, using the following technique. Firstly, plots of $|S_{21}|$, in the vicinity of f_0 and f_l, are presented. These plots show (i) the mean value of $|S_{21}|$; (ii) the maximum value of $|S_{21}|$, where the maximum value is derived from the mean value plus its standard uncertainty [37]; and (iii) the minimum value of $|S_{21}|$, where the minimum value is derived from the mean value minus its standard uncertainty [37]. These plots are shown in Figs. 16 and 17 for f_0, and f_l respectively; is f_u calculated the same way as f_l but from the upper 3 dB point.

Following the methods described in [32] the mean values and standard uncertainties in f_0, f_l and f_u are used in Eqs. (4)–(7) to obtain the standard uncertainty in Q_L, $u(Q_L)$. This gives a value of $Q_L = 4\,129 \pm 58$; which gives an uncertainty in Q_L of 1.4%.

$$u(Q_L) = \sqrt{\left(\frac{\partial Q_L}{\partial f_0}\right)^2 u(f_0)^2 + \left(\frac{\partial Q_L}{\partial f_l}\right)^2 u(f_l)^2 + \left(\frac{\partial Q_L}{\partial f_u}\right)^2 u(f_u)^2} \quad (4)$$

$$\frac{\partial Q_L}{\partial f_0} = \frac{1}{f_u - f_l} \quad (5)$$

$$\frac{\partial Q_L}{\partial f_u} = \frac{-f_0}{(f_u - f_l)^2} \quad (6)$$

$$\frac{\partial Q_L}{\partial f_l} = \frac{f_0}{(f_u - f_l)^2} \quad (7)$$

The mean values and standard uncertainties for Q_L and $|S_{21}|$ are then used in Eqs. (8)–(10) to obtain the standard uncertainty in Q_0, $u(Q_0)$.

$$u(Q_0) = \sqrt{\left(\frac{\partial Q_0}{\partial Q_L}\right)^2 u(Q_l)^2 + \left(\frac{\partial Q_0}{\partial |S_{21}|}\right)^2 u(|S_{21}|)^2} \quad (8)$$

$$\frac{\partial Q_0}{\partial Q_L} = \frac{1}{1 - |S_{21}|} \quad (9)$$

$$\frac{\partial Q_0}{\partial |S_{21}|} = \frac{Q_L}{(1 - |S_{21}|)^2} \quad (10)$$

This gives a value of $Q_0 = 8\,460 \pm 120$; which gives an uncertainty in Q_0 of 1.4%

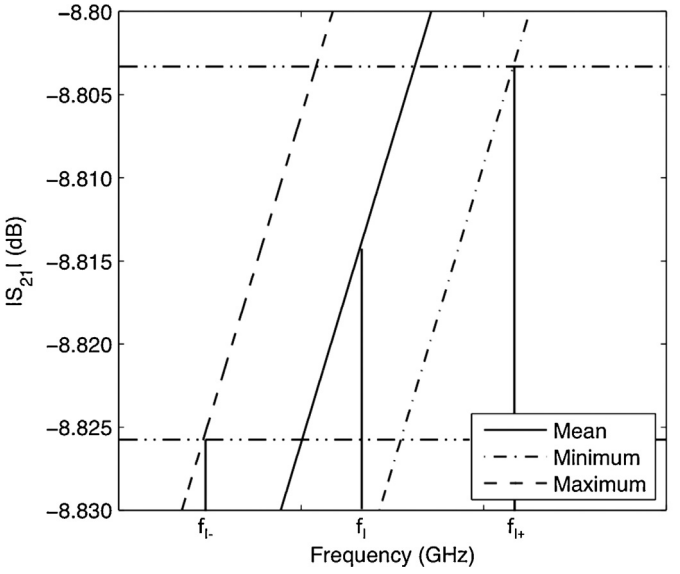

Fig. 17. Impact of uncertainty in $|S_{21}|$ on the determination of f_l for the strongly-coupled inline PC resonator.

6.2. Uncertainty analysis for phase Q-factor determination

We next consider a second method of propagating the uncertainty in the *S*-parameter measurements when the Q-factor is determined using the phase of S_{21}, as described by Eq. (2). The maximum and minimum values of ω_0 are found using the same method as described using Fig. 16 (with the value of f_0 found by converting to angular frequency ω_0). Uncertainty in the phase gradient is determined by plotting the mean, maximum and minimum values of $\angle S_{21}$, as shown in Fig. 18. These minimum and maximum curves are found by taking the mean and then adding or subtracting the standard uncertainty in the measurement of the phase. To establish the uncertainty in the phase gradient, three gradients are taken,

Table 4
Summary Q-factor values with uncertainties.

Q-factor method	Q_L	Q_0
3 dB	4129 ± 116	8460 ± 240
Phase	4412 ± 144	9040 ± 300

using a finite difference method: (i) from the mean value curve at f_{0-}, and f_{0+}; (ii) the maximum curve at f_{0-} and minimum curve at f_{0+}; and (iii) the minimum curve at f_{0-} and maximum curve at f_{0+}, where f_{0-}, and f_{0+} are the measured values either side of the peak f_0.

These values are then applied to Eq. (2), to find the mean Q_L from the mean values of ω_0 and $\left|\frac{\delta\angle S_{21}}{\delta\omega}\right|$. The standard uncertainty in Q_L, due to $u(Q_{L\omega_0})$, is calculated using the maximum and minimum of ω_0, whilst keeping $\left|\frac{\delta\angle S_{21}}{\delta\omega}\right|$ at its mean value, giving $u(Q_{L\omega_0}) = \pm 37$. The same method is employed to calculate the standard uncertainty in Q_L due to $\left|\frac{\delta\angle S_{21}}{\delta\omega}\right|$, $u(Q_{L\angle})$, keeping ω_0 constant at its mean value and then applying the maximum and minimum values for $\left|\frac{\delta\angle S_{21}}{\delta\omega}\right|$. This gives $(uQ_{L\angle}) = \pm 63$.

Finally, Eq. (11) is used to obtain $(uQ_L) = \pm 72$, thus, giving $Q_L = 4412 \pm 72$.

$$u(Q_L) = \sqrt{u(Q_{L\omega_0})^2 + u(Q_{L\angle})^2} \tag{11}$$

To obtain Q_0 and $u(Q_0)$ the same method, as used previously in Eqs. (8)–(10), is used to give $Q_0 = 9040 \pm 150$; this gives an uncertainty in Q_L of 1.6% and 1.7% in Q_0. As with all the calculated Q-factors presented in this section, the deviation from the numbers given in Tables 2 and 3 may be slightly larger than the uncertainties calculated. This is due to Type A uncertainties being intentionally neglected, as it quantifies alignment limitations in our experimental setup and not the underlying performance of the PC resonators.

Finally, Table 4 provides a summary of the obtained loaded and unloaded Q-factor values, using both calculation methods; '3 dB' and 'phase'. The uncertainties given in this Table are expanded uncertainties, providing an uncertainty interval at a level of confidence of 95% [37]. Each expanded uncertainty, U_{Q_L} and U_{Q_0}, is obtained by multiplying the previously obtained standard uncertainties, $u(Q_L)$ and $u(Q_0)$, as calculated in this paper, by a coverage factor, ς:

$$U_{QL} = \varsigma u(Q_L) \quad \text{and} \quad U_{Q_0} = \varsigma u(Q_0) \tag{12}$$

On this occasion, for both expanded uncertainties, a value of $\varsigma = 2$ is chosen to provide the required 95% level of confidence.

7. Conclusions

In this paper, the fabrication and measurement of three W-band ultra-high Q-factor PC resonators has been presented. The manufacturing method using standard microfabrication techniques has been described. A detailed analysis of the experimental results and a technique of propagating uncertainty from measured *S*-parameters to unloaded Q-factor have been presented for the first time. Using this unique technique, it is shown that the strongly-coupled inline PC resonator has an unloaded Q-factor of $Q_0 = 9040 \pm 300$, which is a factor of 3 higher than that for a comparable whispering gallery dielectric resonator at the same frequency. The inherent physical limitation on the unloaded Q-factor has been shown through numerical simulations to be determined by the dielectric absorption losses within HRS to be $Q_0 \sim 10\,000$ (assuming a resistivity 10 kΩ cm).

As pointed out in the Introduction, high Q-factor resonators play a vital role in achieving greater performance in many practical applications. For example, there is a clear relationship between Q-factor and performance in oscillators [7] and filters [27]. Moreover, in spectroscopy, spectral resolution is ultimately inversely proportional to the −3 dB bandwidth of the resonators used; this means that it is directly proportional to the unloaded Q-factor, as given by Eqs. (1) and (3). From another perspective, with perturbation techniques, the refractive index of a test sample interacting with the fields of the resonator will produce a wavelength shift that is proportional to the unloaded Q-factor [38]. Future work is concentrating on how to integrate microfluidic channels on the silicon wafer to allow gas and liquid analytes to be sensed for future millimeter-wave lab-on-a-chip applications.

Acknowledgments

This work was supported in part by the Leverhulme Trust, the UK's Engineering and Physical Sciences Research Council (EPSRC) under Platform Grant EP/E063500/1, the Val O'Donoghue Scholarship in Electrical and Electronic Engineering and the National Measurement Office of the UK Government's Department for Business, Innovation & Skills.

The authors would like to thank P. McCluskey at Rhode and Schwarz, for the loan of their W-band VNA in our initial experiments. In addition, Dr. M. M. Ahmad, Dr. A. Delahunty, Dr. R. J. Hergert, Dr. W. J. Karl and Dr. S. W. Wright, for their guidance in micromachining.

References

[1] P.H. Siegel, Terahertz technology, IEEE Trans. Microw. Theory Tech. 50 (March (3)) (2002) 910–928.
[2] E.N. Shaforost, N. Klein, S.A. Vitusevich, A. Offenhäusser, A.A. Barannik, Nanoliter liquid characterization by open whispering-gallery mode dielectric resonators at millimeter wave frequencies, J. Appl. Phys. 104 (October (7)) (2008) 074111.
[3] H. Kurt, D. Citrin, Coupled-resonator optical waveguides for biochemical sensing of nanoliter volumes of analyte in the terahertz region, Appl. Phys. Lett. 87 (December (24)) (2005) 241119.
[4] Y. Zhao, Y. Li, B. Pan, S.-H. Kim, Z. Liu, M.M. Tentzeris, J. Papapolymerou, M.G. Allen, RF evanescent-mode cavity resonator for passive wireless sensor applications", Sensor Actuator A: Phys. 161 (June (1)) (2010) 322–328.
[5] S. Lucyszyn, Y. Zhou, Characterising room temperature THz metal shielding using the engineering approach, PIER J. 103 (2010) 17–31.
[6] Y. Zhou, S. Lucyszyn, Modelling of reconfigurable terahertz integrated architecture (RETINA) SIW structures, PIER J. 105 (2010) 71–92.
[7] I.D. Robertson, S. Lucyszyn (Eds.), RFIC and MMIC Design and Technology, IET, London, 2001.
[8] S.S.H. Hsu, H.-Z. Zhu, W-band multiple-ring resonator by standard 0.18-μm CMOS technology, IEEE Microw. Wireless Compon. Lett. 15 (December (12)) (2005) 832–834.
[9] B. Temelkuran, M. Bayindir, E. Ozbay, J.P. Kavanaugh, M.M. Sigalas, G. Tuttle, Quasimetallic silicon micromachined photonic crystals, Appl. Phys. Lett. 78 (January (3)) (2001) 264–266.
[10] S. Song, K.-S. Seo, A W-band air-cavity filter integrated on a thin-film substrate, IEEE Microw. Wireless Compon. Lett. 19 (April (4)) (2009) 200–202.
[11] P. Blondy, D. Cros, P. Guillon, F. Balleras, C. Massit, W band silicon dielectric resonator for semiconductor substrate characterization, IEEE MTT-S Int. Microw. Symp. Dig. June (3) (1998) 1349–1352.
[12] Y. Akahane, T. Asano, B.S. Song, S. Noda, High-Q photonic nanocavity in a two-dimensional photonic crystal, Nature October (425) (2003) 944–947.
[13] Y. Zhao, Y.-N. Zhang, Q. Wang, Research advances of photonic crystal gas and liquid sensors, Sensor Actuator B: Chem. 160 (December (1)) (2011) 1288–1297.
[14] A. Di Falco, L. O'Faolain, T.F. Krauss, Chemical sensing in slotted photonic crystal heterostructure cavities, Appl. Phys. Lett. 94 (2009).
[15] D. Biallo, A. D'Orazio, M. De Sario, V. Marrocco, V. Petruzzelli, F. Prudenzano, Photonic Crystal Sensors, Int. Conf. Transpar. Optical Netw. June (2) (2006) 44–48.
[16] M. Schuster, N. Klein, P. Ruther, A. Trautmann, O. Paul, P. Kuzel, F. Kadlec, An interconnected 2D-TM EBG structure for millimeter and submillimeter waves, IEEE J. Sel. Areas Commun. 23 (July (7)) (2005) 1378–1384.
[17] S.W.H. Tse, P.R. Young, Photonic crystal non-radiative dielectric waveguide, IEEE MTT-S Int. Microw. Symp. Dig. (June) (2005) 1079–1081.

[18] W.J. Otter, S.M. Hanham, E. Episkopou, Y. Zhou, N. Klein, A.S. Holmes, S. Lucyszyn, Photoconductive photonic crystal switch, September, in: Infrared, Millimeter, and Terahertz Waves (IRMMW-THz), 38th International Conference, 2013.
[19] L. Mingyu, N.W. Chen, J.W. Bredow, S. Jung, S. Tjuatja, Study of photonic crystals at millimeter wave band, IEEE Antenna Propag. Soc. Int. Symp. (June) (2007) 177–180.
[20] X. Hao, A. Higgins, M. Kim, Tunable millimeter-wave band-stop filter using electromagnetic crystal (EMXT) surfaces, IEEE Antenna Propag. Soc. Int. Symp. 2 (June) (2003) 1107–1110.
[21] J.D. Joannopoulos, S.G. Johnson, Photonic Crystals: Molding the Flow of Light, Princeton University Press, Princeton, NJ, 2008.
[22] J.W. Lamb, Miscellaneous data on materials for millimetre and submillimetre optics, Int. J. Infrared Millimet. Waves 17 (September (12)) (1996) 1997–2034.
[23] S. G. Johnson, MIT Photonics-Bands (MPB). Available: http://ab-anitio.mit.edu/wiki/index.php/MIT_Photonic_Bands
[24] D. Englund, I. Fushman, J. Vučković, General recipe for designing photonic crystal cavities, Opt. Express 13 (August) (2005) 5961–5975.
[25] D. Kajfez, Pierre Guillon, Dielectric Resonators, 2nd ed., SciTech Publishing Inc., 1998, July.
[26] Waveguides Rigid, Rectangular (millimetre wavelength) MIL-DTL-85/3C, 2005, October.
[27] S. Lucyszyn (Ed.), Advanced RF MEMS, Cambridge University Press, Cambridge, 2010.
[28] S. Kumar, Design and fabrication of micromachined silicon suspensions, Ph.D. Dissertation, Dept. Elect. Eng., Imperial College London, UK, 2007.
[29] S. Hadzialic, S. Kim, A.S. Sudbø, O. Solguard, Two-dimensional photonic crystals fabricated in monolithic single-crystal silicon, IEEE Photon. Technol. Lett. 22 (January (2)) (2010) 67–69.
[30] G.F. Engen, C.A. Hoer, Thru-Reflect-Line: an improved technique for calibrating the dual six-port automatic network analyser, IEEE Trans. Microw. Theory Tech. 12 (December(12)) (1979) 987–993.
[31] A. Rumiantsev, N.M. Ridler, VNA calibration, IEEE Microw. Mag. 9 (June (3)) (2008) 86–99.
[32] N.M. Ridler, A review of existing national measurement standards for RF and microwave impedance parameters in the UK, IEE Colloq. (1999), Dig., no. 99/008, pp 6/1–6/6, February.
[33] N.M. Ridler, News in RF Impedance Measurement, XXVIIth General Assembly of the International Union of Radio Science (URSI), Maastricht, The Netherlands, 2002.
[34] G.J. French, N.M. Ridler, A primary national standard for millimetric waveguide S-parameter measurements, Microw. Eng. Eur. (1999 Oct) 29–32.
[35] High Resistivity (HiRes™) Silicon for GHz and THz Technology, Application note version 1.1, Topsil, 2014, January.
[36] Guidelines of the Evaluation of Vector Network Analysers (VNA), EURAMET cg-12 Version 2.0 (03/2011).
[37] JCGM 100:2008, Evaluation of measurement data – Guide to the expression of uncertainty in measurement, First ed., 2008, September, http://www.bipm.org
[38] E. Episkopou, S. Papantonis, W.J. Otter, S. Lucyszyn, Defining material parameters in commercial EM solvers for arbitrary metal-based THz structures, IEEE Trans. Terahertz Sci. Technol. 2 (September (5)) (2012) 513–524.

Biographies

William J. Otter received the ME degree from Imperial College London in 2010. During this period he undertook industrial placements at BAE Systems, Advanced Technology Centre, Great Baddow, UK. He is currently a research assistant in the area of RF ambient energy harvesting at Imperial College London and working on a Ph.D. degree from Imperial College London. His research interests include electromagnetics, filter design, optoelectronics and terahertz and microwave sensors. He holds the Val O'Donoghue Scholarship in the Deparment of Electrical and Electronic Engineering.

Stephen M. Hanham received the B.E. and B.Sc. degrees from the University of Western Australia, Perth, Australia in 2004 and the Ph.D. degree from the University of Sydney, Australia in 2010. From 2008 to 2010 he was a research project officer and later a systems engineer at the Commonwealth Scientific and Industrial Research Organization (CSIRO) in Sydney, Australia working on THz antennas and detectors as well as mobile satellite systems. Currently, he is working at Imperial College London, UK as a research associate in the area of near-field terahertz imaging, spectroscopy and plasmonics. His research interests include electromagnetics, plasmonics, antennas and terahertz and microwave technologies.

Nick M. Ridler received the B.Sc. degree from the University of London, UK, in 1981. He has since spent more than 30 years working in both industrial and government scientific research laboratories. He is currently employed by the National Physical Laboratory, UK, where he is a principal research scientist involved in high-frequency precision measurement activities. His current research interests include measurements at millimeter and sub-millimeter wavelengths and high-speed digital signal measurements on printed circuit boards. Ridler was the President (2011–2013) of ARFTG (the Automatic RF Techniques Group); Past Chair (2010–2012) of the IEEE MTT-11 "Microwave Measurements" Technical Committee; Chair of IEEE Standard Working Group P1785 "Waveguide for Millimeter and Submillimeter Wavelengths"; Vice-chair of IEEE Standard Working Group P287 "Precision Coaxial Connectors at RF, Microwave and Millimeter-wave Frequencies"; Vice-chair of the MTT-S Standards Coordinating Committee; and, Member of the IEEE MTT-4 "Terahertz Technology and Applications" Technical Committee. He is a chartered engineer (CEng), fellow of the Institution of Engineering and Technology (FIET) and Fellow of the Institute of Electrical and Electronics Engineers (FIEEE).

Giuseppe Marino received the B.Sc. and M.Sc. degrees in 2009 and 2012 from the University of Catania, Italy. From February to August 2011 he was an Erasmus student at Imperial College London working on GHz and THz antennas and detectors. Currently, he is working at King's College London, UK as a Ph.D. student in the area of non-linear processes in plasmonic metamaterial.

Norbert Klein is full professor and chair in Electromagnetic Materials at Imperial College London and director of Imperial's Centre of Terahertz Science and Engineering. Before 2009, Prof. Klein was division leader for Electromagnetic Sensors at Juelich Research Center in Germany and was lecturing at Technical Universities of Aachen and Dortmund in Germany. He is (co)author or more than 160 peer-reviewed scientific papers and book articles and is key inventor in more than 10 European and US patents related to microwave devices for sensor-and communication applications. In 2007 Prof. Klein founded a spin off company which has successfully commercialized a microwave sensor system for airport security. His current research activities comprise microwave and terahertz sensors for biomedical and security applications and low-dimensional nanomaterials for high frequency applications.

Stepan Lucyszyn is currently a Reader (associate professor) in Millimeter-wave Electronics and Director of the Centre for Terahertz Science and Engineering, at Imperial College London. Dr. Lucyszyn has (co-)authored over 160 papers and 12 book chapters in applied physics and electronic engineering, and delivered many invited presentations at international conferences. He was the Chairman of the 41st European Microwave Conference, held in Manchester (UK, 2011). He was an IEEE distinguished microwave lecturer (DML) for 2010–12, Emeritus DML for 2013 and appointed an EuMA European Microwave Lecturer (EML) for 2013–present. Dr. Lucyszyn is a fellow of the Institute of Physics (UK, 2005), Institution of Engineering and Technology (UK, 2005), The Electromagnetics Academy (USA, 2008) and Institute of Electrical and Electronic Engineers (USA, 2014). He is one of the academic co-founders of the Imperial College London spin-out company Drayson Wireless Limited, established Apr. 2014.